Quasi-online failure times identification of mobile heat sources in 2D geometry

Mohamed Salim Bidou, L. Perez, Sylvain Verron, Laurent Autrique

Journal of Process Control 136 (2024) 103183

Contents lists available at ScienceDirect

Journal of Process Control

journal homepage: www.elsevier.com/locate/jprocont

Quasi-online failure times identification of mobile heat sources in 2D geometry

M.S. Bidou *, L. Perez, S. Verron, L. Autrique

LARIS, Polytech, University of Angers, 62 avenue notre dame du lac, 49000 Angers, France

ARTICLE INFO

Keywords:
Failure time identification
Failure diagnosis
Online parameters estimation
Conjugate gradient method
Kalman filters
Inverse problem
Partial differential equations

ABSTRACT

Identifying the failure instants in thermal systems subject to 2D parabolic partial differential equations presents a significant challenge, especially when the systems involve mobile heat sources. In the context of this study, mobile heat sources are examined, along with a set of stationary sensors, while assuming known and constant-velocity trajectories for the heat sources. This research introduces a quasi-online methodology that incorporates Exponentially Weighted Moving Average (EWMA) charts for immediate failure detection. When a failure is detected via the EWMA charts, the Conjugate Gradient Method, traditionally developed for offline applications, is activated. This method is adapted to a quasi-online framework, facilitating a more rapid and precise identification of malfunctioning heat sources, the exact time of their failures, and the possibility of restoring normal operations. To assess the performance and reliability of this approach, it is compared with a Bayesian filter-based method, particularly using the Kalman filter for this purpose. Monte Carlo simulations are employed to evaluate the resilience and effectiveness of the quasi-online method, focusing on the system's sensitivity to the accuracy of sensor measurements.

1. Introduction

Given the increasing complexity of industrial plants and the growing importance attached to their safe operation, fault diagnosis has received particular attention in recent years. The application of models based on partial differential equations (PDEs) is now widely used to capture various physical behaviors in these complex systems. For example, the dynamics of thermal systems, governed by heat transfer principles, often translate into parabolic PDEs. Conventional ordinary differential equations (ODEs) often fail to provide accurate representations of real-world engineering systems, as they lack the ability to simultaneously account for spatial and temporal changes. Consequently, model-based methodologies for fault identification and analysis have become effective tools for overcoming these limitations. In this context, faults are defined as malfunctions in system components, sensor equipment or control devices. If these problems are not detected and rectified early, system efficiency can be significantly reduced, leading to catastrophic failures or major losses, both human and material. Therefore, rapid and accurate fault identification is essential to ensure system reliability and minimize undesirable outcomes.

In systems designed for industrial heating, heat source malfunctions can lead to reduced operational efficiency, lower product quality and safety issues. For heating, ventilation and air-conditioning (HVAC) systems, accurately pinpointing when failures occur is essential to maintaining thermal consistency, energy-saving operations and user comfort. Power generation facilities rely heavily on reliable heating sources, and any malfunction can lead to interruptions in electricity supply or reduced performance. In solar thermal systems, which harness the sun's energy for heating, reliable fault recognition is imperative to optimize energy yields. Industries with specialized processes, such as the petrochemical or food industries, depend on the performance of thermal systems. In such cases, immediate identification of operational problems is vital to meet production deadlines, guarantee production quality and avoid safety-related incidents.

Research on the control and estimation of PDEs has been an active area for several decades. Generally, there are two primary approaches for PDEs control and estimating: (1) Early lumping, which involves converting PDEs to ODEs and performing the design in a finite-dimensional space [1,2]; and (2) Late lumping, which involves designing in an infinite-dimensional space and directly studying the PDEs without using approximate methods [3,4]. While significant focus has been given to control and estimation studies, the subject of system fault diagnosis in the context of PDEs has been relatively less explored. Existing PDEs diagnostic schemes mainly employ early lumping approaches [5–9]. The early lumping method has been extensively employed in early research on system fault diagnosis utilizing PDEs modeling. Nevertheless, this approach suffers from certain drawbacks. It simplifies

* Corresponding author.
E-mail address: mohamedsalim.bidou@univ-angers.fr (M.S. Bidou).

https://doi.org/10.1016/j.jprocont.2024.103183
Received 14 October 2023; Received in revised form 11 February 2024; Accepted 15 February 2024
Available online 17 February 2024

Nomenclature

Δt	time step, s
Δt_{obs}	time step of the observations, s
$\Delta x, \Delta y$	space step, m
λ	thermal conductivity, W m^{-1} K^{-1}
$\vec{n}$	unit external outward-pointing vector
ρC	volumetric heat, J m^{-3} K^{-1}
e	thickness, m
h	natural convection coefficient, W m^{-2} K^{-1}
T	temperature, K
t	time, s
t_f	final time, s
T_0	initial temperature, K
x	space variable, m
y	space variable, m

PDEs into ODEs, leading to a partial and often inaccurate capture of system dynamics. While PDEs capture complex phenomena such as diffusion and convection, these are inadequately represented in the simpler ODE format. In addition, system failures alter the dynamics of PDEs, further reducing the accuracy and reliability of the ODE model for failure detection, as they do not fully account for changes in the interactions between variables. The other "late lumping" based on PDEs observer-based fault diagnosis schemes has been successfully applied to parabolic systems in research projects. In [10], a model-based fault detection, estimation, and prediction scheme is developed for linear distributed parameter systems. [11] introduces a method for abnormality localization in linear parabolic DPSs, utilizing a mix of in-domain and boundary measurements along with backstepping techniques to improve detection and localization accuracy. The study in [12] focuses on spatiotemporal fault detection in nonlinear reaction–diffusion equations, employing an observer-based approach for fault detection and estimation, complemented by feedback control, with the methodology's effectiveness validated through simulation. Finally, [13] offers a comprehensive analysis of fault detection and isolation in both linear and nonlinear distributed parameter systems, using filter-based observers for linear systems and Luenberger-type observers for nonlinear systems. This approach particularly emphasizes isolating actuator, sensor, and state faults, with its efficacy demonstrated through simulation.

This article presents a methodology for identifying failure times in heating sources within a thermal system using a parametric identification method. Within this framework, it is reasonable to consider the search for failures in a system governed by a PDE system under normal conditions as an inverse problem [14]. Consequently, in the thermal domain, a gradient conjugate method is employed to solve Inverse Heat Conduction Problems (IHCPs). However, IHCPs are mathematically ill-posed, as it is challenging to satisfy the requirements of existence, uniqueness, and continuity simultaneously. This ill-posedness is exacerbated by the sensitivity of IHCPs to random errors in measurement, leading to significant inaccuracies in the numerical solutions. Several methods have been proposed to tackle IHCPs, including the Tikhonov regularization method [15,16], the sequential function specification method [17,18], the iterative regularization method [19,20] and the Bayesian methods [21,22].

In [23], an iterative conjugate gradient regularization approach was used to determine the heat transfer coefficient in a two-dimensional transient heat conduction scenario. Similarly in [24], the same method was applied to predict the heat transfer coefficient at the inner wall of a nuclear power plant pipeline responsible for transporting a mixture of warm and cold fluids. Another study conducted by [25], focused on the estimation of surface heat flux in three-dimensional IHCP. Additionally, [26] proposed an adaptive selection of relevant sensors within a network was proposed to estimate an unknown mobile heating flux, optimizing the sensor configuration to enhance the accuracy of the estimation. Furthermore, in [27], a novel data-driven structure was introduced to enable direct analysis and parameter inversion of heat conduction problems (HCPs). This approach leverages available data to directly infer the parameters of the heat conduction model, facilitating efficient analysis and estimation.

When it comes to the identification of failure times in a system governed by PDEs, the failure instants within the thermal framework can be identified by solving IHCPs based on observations from the malfunctioning system. However, it is crucial to address some important considerations in the fault diagnosis process. Firstly, IHCPs are highly sensitive to measurement errors due to their ill-posed nature [28]. Additionally, the failures being investigated are characterized as "on-off" events, and the study's structure shares similarities with hybrid systems that involve delays caused by discontinuous switching associated with heat transport phenomena.

In our prior research [14], we introduced a method for the effective diagnosis of failures in stationary heat source systems, effective even in the presence of noisy data in offline contexts. This technique is particularly effective in accurately identifying malfunctioning heat sources, accurately determining the moment of failure, and potentially enable the restoration of normal operations. We have achieved this by presenting the identification process as a quadratic criterion minimization problem, solved by an iterative regularization approach.

However, a key limitation of this offline method is the necessity to wait until the completion of the experimental phase to begin diagnosing failures. This delay restricts the ability to take timely corrective actions, reducing the scope for immediate intervention. To address this, our current research proposes a quasi-real-time strategy for identifying mobile heat source failures. This approach relies on the exponentially weighted moving average (EWMA) control chart, mentioned in [29], as an essential tool for fast detection. The EWMA control chart, a statistical method for tracking the evolution of processes over time, plays an essential role in our context. In the event of a heat source malfunction, sensor residuals (differences between actual and expected values under normal conditions) exceed thresholds predefined on the EWMA chart. This triggers the identification process, which we then carry out using the Conjugate Gradient Method (CGM).

The approach involves two main stages:

- Real-time, failure detection using the EWMA control chart technique.
- Subsequent identification using the CGM algorithm.

The structure of this article is organized as follows. Section 2 provides a detailed description of the physical problem formulation in two-dimensional geometry. Section 3 introduces a quasi-online diagnostic framework that integrates real-time failure detection, specifically utilizing the EWMA control chart, and subsequent failure identification. The section further explores two distinct methodologies for failure identification. The first employs an adapted version of the conjugate gradient iterative regularization method, with a focus on precisely defining moments of failure and recovery for heating sources. The second utilizes a Bayesian approach, incorporating Kalman filters and smoothers to estimate heat source intensities, and introduces techniques to estimate failure and restart timings. It is important to note that this second approach serves as a comparative study with the first, with the aim of enriching our understanding and broadening the scope of our investigation. Numerical results are presented and discussed in Section 4. Finally, Section 5 presents the conclusion and the perspectives offered by this work.

2. Application description

2.1. The direct problem

General Context: In the study of thermal systems governed by parabolic partial differential equations, the direct problem typically involves understanding the dynamics of heat flux within a defined geometric domain. For thin material, this domain, Ω, encompasses various points in space, each with its unique coordinates (x, y). The boundary of this domain is denoted as Γ. Within this context, $T(x, y, t)$ represents the temperature at any given point and time, evolving as per the system's governing equations.

A general formulation of the direct problem can be expressed as follows, where the temperature's temporal evolution in the domain Ω is governed by a set of linear parabolic partial differential equations [30]:

$$\begin{cases} \rho C \dfrac{\partial T(x,y,t)}{\partial t} - \lambda \Delta T(x,y,t) = \\ \qquad\qquad \dfrac{\mathrm{q}(x,y,t) - 2h\left(T(x,y,t) - T_{\text{ambient}}(x,y)\right)}{e}, \\ T(x,y,0) = T_0(x,y), \quad (x,y) \in \Omega, \\ -\lambda \dfrac{\partial T(x,y,t)}{\partial \vec{n}} = 0, \quad (x,y,t) \in \Gamma \times \left[0, t_f\right], \end{cases} \tag{1}$$

where Δ is the Laplacian operator:

$$\Delta T(x,y,t) = \frac{\partial^2 T(x,y,t)}{\partial^2 x} + \frac{\partial^2 T(x,y,t)}{\partial^2 y}.$$

Material thickness is denoted by e. Thermophysical properties of the material are denoted by ρC the volumetric heat and λ the thermal conductivity. Thermal exchanges with the surrounding are governed by convective exchanges : h is the convective exchange coefficient while T_{ambient} is the ambient temperature and $T_0(x, y)$ represents the non-uniform initial temperature profile, which is a function of spatial coordinates (x, y). The total amount of heat flux $\mathrm{q}(x, y, t)$ is determined by the collective contribution of several distinct heating sources. Mathematically, the heat flux at a given point (x, y, t) is the sum of individual heat fluxes generated by each source, denoted as $\mathrm{q}_i(x, y, t)$, where i ranges from 1 to n_{heat} :

$$\mathrm{q}(x,y,t) = \sum_{i=1}^{n_{\text{heat}}} \mathrm{q}_i(x,y,t). \tag{2}$$

These heat sources exhibit spatially varying distributions and temporal characteristics. Each heat source, $\mathrm{q}_i(x, y, t)$, can be described by the product of three separate functions:

$$\mathrm{q}_i(x,y,t) = \psi_i(x,y,t)\phi_i(t)\varrho_i(t), \tag{3}$$

where $\psi_i(x, y, t)$, determines the spatial support; $\phi_i(t)$, defining the temporal heat flux behavior; and $\varrho_i(t)$, indicating the operational state of the source.

Specific Scenario: In our specific application, we examine a 1 meter long by 1 meter wide by 2 mm thick aluminum plate. On this are positioned four temperature sensors and three heating sources, $n_{\text{heat}} = 3$. The three sources and four sensors in our system are positioned at known locations. These sources are prone to all-or-nothing failures, characterized by sudden cessation of function (resulting in zero heat flux), followed by a return to their normal operational state. Fig. 1 visually depicts the placement of these sources and sensors within the system. The sensors employed are primarily of the pointwise type, strategically designed to provide precise, localized measurements.

The geometric domain is defined as $\Omega = [-0.5, 0.5]^2 \subset \Re^2$, every point in space possesses its own coordinates $(x, y) \in \Omega$. $t \in \left[0, t_f\right]$ is the time variable. The initial temperature condition across the plate is uniformly set at $T_0 = 293$ K. The input parameters for the model are listed in Table 1, and it is important to note that these parameters remain constant regardless of the temperature T.

Table 1
Mathematical model input parameters.

Symbol	Definition	Values
ρC	Volumetric heat	$2.421.10^6$ J m^{-3} K^{-1}
h	Natural convection coefficient	10 W m^{-2} K^{-1}
λ	Thermal conductivity	178 W m^{-1} K^{-1}
T_0	Initial temperature	293 K
t_f	Final time	3600 s
e	Thickness	$2 \cdot 10^{-3}$ m

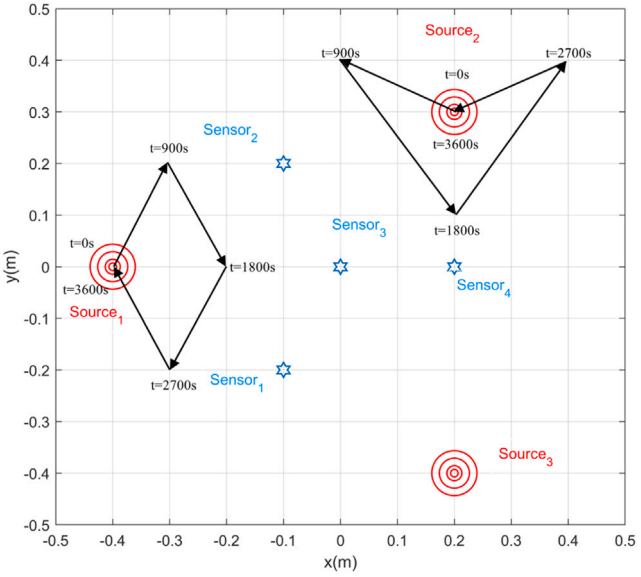

Fig. 1. Positions of the plate's 3 sources and 4 sensors.

The function $\psi_i(x, y, t)$ determines the spatial support of the heat source and represents its spatial distribution. It is modeled as a Gaussian distribution centered at the point $(x_i(t), y_i(t))$:

$$\psi_i(x,y,t) = \exp\left(-\frac{\left(x - x_i(t)\right)^2 + \left(y - y_i(t)\right)^2}{\left(5 \times 10^{-2}\right)^2}\right). \tag{4}$$

The temporal behavior of each heat source is captured by the function $\phi_i(t)$, which represents the normal heating flux generated by the source i. This function provides information about how the heat flux varies over time for each individual source. To provide a visual representation of the heat flux dynamics, Fig. 2 displays the evolution of the heat flux for the three sources over time.

2.2. Failure description

The failures being investigated can be classified as all-or-nothing failures. This means that a heating source has a binary behavior: it can either be in an operational state or a non-operational state. Specifically, when a failure occurs, the source stops operating, leading to a complete absence of heat flux, which is represented as a value of zero. Subsequently, the source has the capability to return to its normal operational behavior. Mathematically, this behavior can be described using the following expression:

$$\varrho_i(t) = \begin{cases} 1 & \text{without failure,} \\ 0 & \text{in case of failure,} \end{cases} \tag{5}$$

where $\varrho_i(t)$ represents the state of source i at time t, with a value of 1 indicating normal operation and a value of 0 indicating failure. An example demonstrating the behavior of the function $\varrho_i(t)$ $i = 1, 2, 3$ is

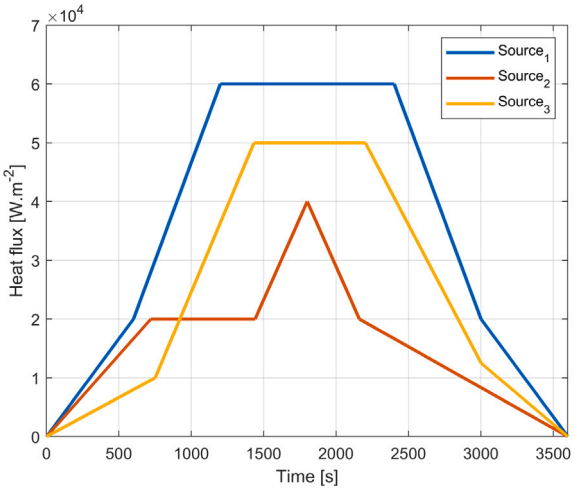

Fig. 2. Flux $\phi_1(t)$, $\phi_2(t)$ and $\phi_3(t)$ of the three sources.

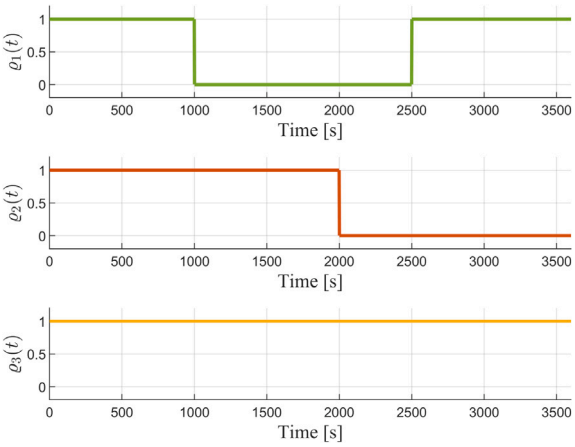

Fig. 3. Illustrations of $\varrho_1(t)$, $\varrho_2(t)$ and $\varrho_3(t)$.

depicted in Fig. 3. In this example, source 1 experiences a failure at 1000 s and restarts operation at 2500 s, source 2 fails at 2000 s, and source 3 operates without any failure.

Using the finite element approach, this previous direct problem defined by (1) can be numerically solved if every model's input parameter are fixed based on Comsol-Multiphysics software interfaced with Matlab (Fig. 4). In Fig. 4, the temperature variation on the plate is presented at a specific time of 3600 s, demonstrating the absence of any failures in the three heat sources. This observation corresponds to their expected and normal behavior.

After presenting the application, the next section focuses on the complex aspects of the quasi-online methodology used to identify heat source failure instants.

3. Quasi-online diagnosis

In this section, the discussion begins by presenting the application of the EWMA control chart for real-time fault detection. This statistical technique facilitates the fast detection of anomalies in the system. Next, the identification process is developed based on the CGM approach. Fig. 5 describes the model-based diagnostic process, which comprises two main phases: failure detection and identification.

3.1. Failure detection

The EWMA control chart [29] is a statistical technique for detecting changes in a process by using exponential weights to assign more significance to recent observations. This enables fast detection of process changes and alerts the operator to take corrective actions. In this application, the EWMA control chart is used to identify instances of system failures or restarts. This detection method involves calculating residuals between simulated temperatures and measured temperatures.

The mathematical formulation of the EWMA control chart is as follows:

$$Z_{t,m} = \zeta\, T_{t,m}^{\text{residual}} + (1-\zeta)\, Z_{(t-1),m} \quad \text{for } t = 1, 2, \ldots, n \text{ and } m = 1, \ldots, 4. \quad (6)$$

where:

- $Z_{0,m}$ is the historical data mean (target) for sensor m.
- $T_{t,m}^{\text{residual}} = T_{t,m}^{\text{measurement}} - T_{t,m}^{\text{model}}$ is the residuals at time t for sensor m.
- n is the number of observations being monitored.
- $0 < \zeta \leq 1$ is the smoothing factor, determining the weight of the observed value in relation to the previous weighted average.

The Upper and Lower Control Limits (UCL and LCL) of the EWMA chart are calculated as follows:

$$\text{UCL} = 3\sigma\sqrt{\frac{\zeta}{2-\zeta}}, \qquad \text{LCL} = -3\sigma\sqrt{\frac{\zeta}{2-\zeta}},$$

where:

- σ is the standard deviation of the noise measurement.

To illustrate this detection process, let us use the example where the q_1 heat source fails at time $t = 1500$ s and the measurements data from the 4 sensors are shown in Fig. 6.

The online detection phase is initiated using the EWMA method. Thus, once the failure has been detected, i.e. when the EWMA control limits are exceeded (as shown in Fig. 7(a)), the identification procedure is launched. Note that in this application, four temperature sensors are used (measurements taken every 9 s), and the assumption is that when three of these sensors exceed the EWMA map limits, the identification procedure is launched (Fig. 7(b)).

The decision to use three sensors as a threshold was taken to balance two critical parameters: sensitivity and specificity. Sensitivity is the system's ability to detect failures early, while specificity is its ability to avoid false alarms. If the system were to initiate the failure identification process when a single sensor exceeded the limits, it would be highly sensitive, but would also produce numerous false alarms. Conversely, waiting for all four sensors to exceed the limits would make the system highly specific but less sensitive, thus delaying failure detection. Thus, choosing three sensors as the threshold offers a calculated compromise, enabling timely detection while minimizing false alarms. Finally, According to EWMA control chart, the detection instant is $t_{\text{detect}} = 1575$ s.

The following section provides a comprehensive overview of the proposed approach for the failure identification and the formulation of the inverse problem, building upon our recent research [14].

3.2. Failure identification by CGM method

3.2.1. The inverse problem formulation

To effectively monitor the operational state of heat source i, a continuous and differentiable function, $\varrho_i(t)$, has been introduced as a state indicator. In contrast to traditional models that may use a simple step function, $\varrho_i(t)$ is designed to smoothly transition from the operational state to the failure state, offering a more nuanced and realistic representation of the source's behavior. This smoothness not only facilitates gradient-based optimization, but also accurately captures the

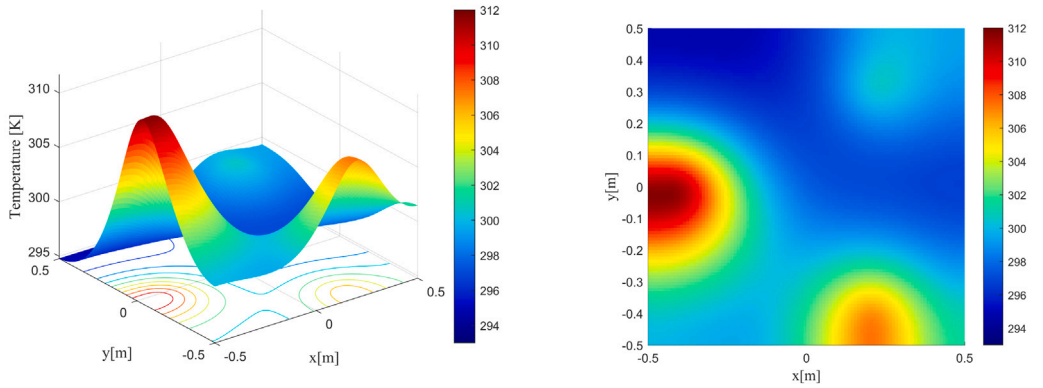

(a) Results of the Direct Problem in 2D Geometry with 3D Visualization

(b) Results of the Direct Problem in 2D Geometry with 2D Visualization

Fig. 4. Solving the direct problem using finite elements method: temperature distribution at t=3600 s under normal operating conditions (no failures).

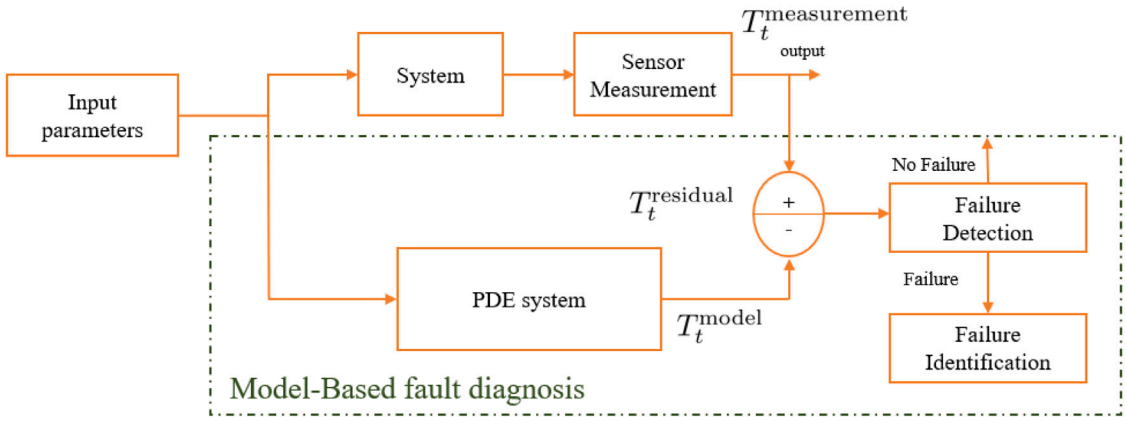

Fig. 5. Scheme of process model-based fault diagnosis steps.

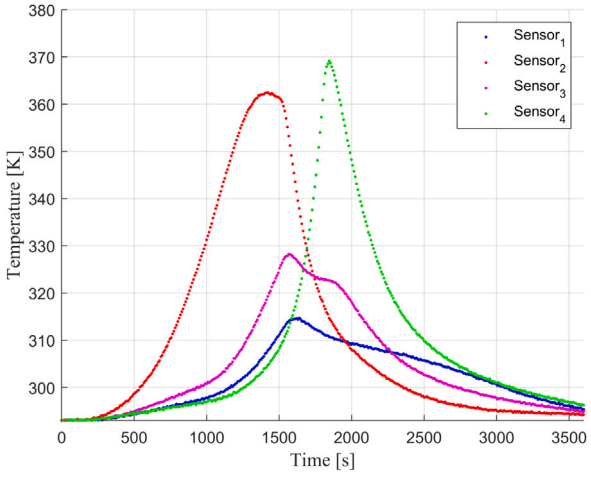

Fig. 6. Measurements data with $\sigma = 0.1$ °C.

subtleties of the source's operational changes. The formulation of $\varrho_i(t)$ takes into account n_i, the total number of failures experienced by the source. It is mathematically defined as:

$$\varrho_i(t) = 1 - \frac{1}{\pi}\sum_{j=1}^{n_i}\left(\operatorname{atan}\left(\frac{t - t^i_{nok,j}}{\eta}\right) - \operatorname{atan}\left(\frac{t - t^i_{ok,j}}{\eta}\right)\right), \tag{7}$$

where $t^i_{nok,j}$ represents the time instants when source i fails (i.e., when $\varrho_i(t)$ transitions from 1 to 0, also known as the falling edge), while $t^i_{ok,j}$ represents the time instants when $\varrho_i(t)$ transitions from 0 to 1 (rising edge). η serves as a smoothing factor that determines the transition width between operational and failure states. The impact of the regularization parameter η is demonstrated in Fig. 8.

The parameter vector that contains unknown parameters is denoted as:

$$\boldsymbol{\tau} = \left[\boldsymbol{\tau}^1, \ldots, \boldsymbol{\tau}^{n_{\text{heat}}}\right], \tag{8}$$

where each component $\boldsymbol{\tau}^i$ is defined as:

$$\boldsymbol{\tau}^i = \left[t^i_{\text{nok},1}, t^i_{\text{ok},1}, \ldots, t^i_{\text{nok},n_i}, t^i_{\text{ok},n_i}\right]. \tag{9}$$

The total number of unidentified parameters is given by $N = \sum_{i=1}^{n_{\text{heat}}}\left(\sum_{j=1}^{n_i} 2n_j\right)$: $\boldsymbol{\tau} = \left(\tau^i_j\right)_{\substack{i=1,\ldots,n_{\text{heat}} \\ j=1,\ldots,2n_i}}$. The odd-indexed components of $\boldsymbol{\tau}$ correspond to failure times, while the even-indexed components correspond to restart times.

To achieve the parametric identification, a technique based on minimizing the output error is employed [31]. The goal is to adjust the undetermined parameters $\boldsymbol{\tau}$ such that the data predicted by the mathematical model aligns with the observed data using a method that has already demonstrated its effectiveness in our prior research [14]. Let $T\left(C_i, t; \boldsymbol{\tau}\right)$ denote the solution of the direct problem (1); that is, the temperature corresponding to a particular value of the unknown τ. The term C_i, where $i = 1, \ldots, 4$, designates the fixed locations of the four sensors within the spatial domain of our thermal system. These locations are defined by coordinates (x_i, y_i) for each sensor and are illustrated in Fig. 1. The sensors at these locations are stationary and provide pointwise temperature observations, denoted by $\hat{T}_i(t)$. In

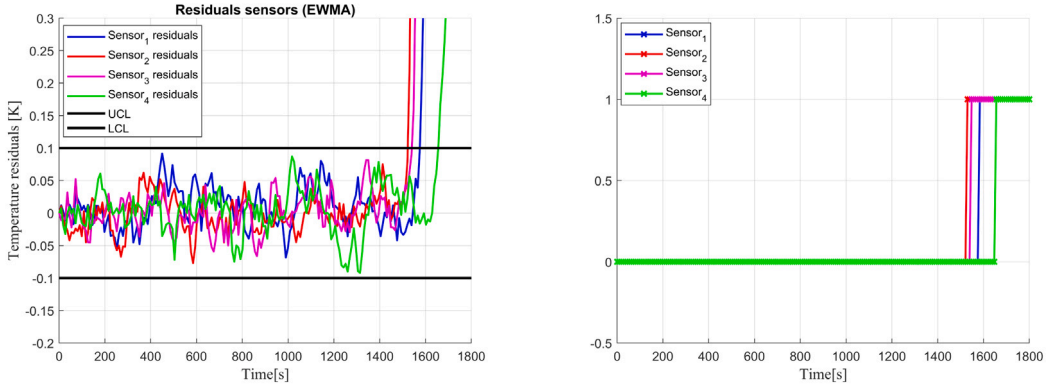

(a) EWMA control chart based on residues: online detection phase.

(b) Decision chart.

Fig. 7. Illustration of online detection for the first failure of source q_1 using the parameters: $\zeta = 0.2$ and $\sigma = 0.1$ °C.

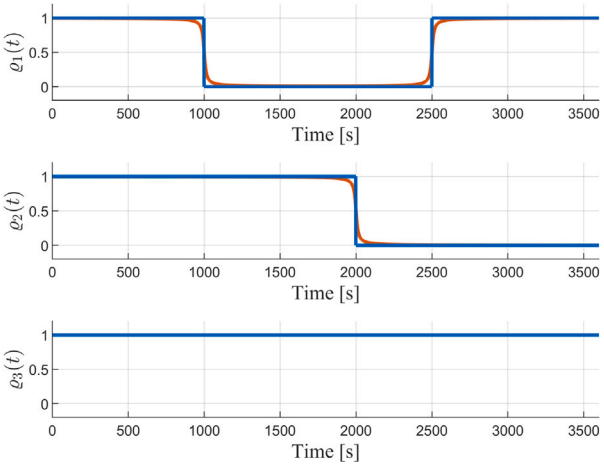

Fig. 8. Illustrations of failures $\varrho_1(t)$, $\varrho_2(t)$ and $\varrho_3(t)$ are provided, with the red curve representing $\eta = 10$ and the blue curve representing $\eta = 0.1$.

addition, the quadratic cost function is expressed as follows:

$$J(\boldsymbol{\tau}) = \frac{1}{2}\sum_{i=1}^{4}\int_0^{t_f}\left(T\left(C_i,t;\boldsymbol{\tau}\right) - \hat{T}_i(t)\right)^2 dt. \tag{10}$$

The criterion $J(\boldsymbol{\tau})$ quantifies the discrepancy between the model predictions and the actual observations, with the aim of minimizing this discrepancy through parameter adjustments. IHCP can be formulated as follows:

- Given: a complete set of input parameters $\left\{e, t_f, \rho C, \lambda, \mathrm{q}, h, T_0\right\}$
- Objective: find the unknown $\boldsymbol{\tau}^*$ such that the quadratic criterion (10) is minimal:

  $$\boldsymbol{\tau}^* = \underset{\boldsymbol{\tau}}{\mathrm{Arg\,min}}\ J(\boldsymbol{\tau}),$$

  subject to the constraint: T is the solution of the direct problem (1).

The identifiability of the optimal solution $\boldsymbol{\tau}^*$ depends not only on the location of the sensors, but also on the parameters and geometric configuration of the system. The unique determination of $\boldsymbol{\tau}^*$ depends on both the precise placement of sensors and the careful selection of system parameters and geometry of the thermal system under study. This realization underlines the need for careful consideration of these factors to ensure the effectiveness and accuracy of the IHCP solution. This complexity of the identifiability process leads us directly to the challenges posed by IHCPs themselves. As ill-posed problems, IHCPs are particularly sensitive to minor measurement perturbations and are prone to significant errors in parameter estimation. In our previous research, we have successfully solved these problems using the conjugate gradient regularization (CGM) method [14]. This iterative algorithm solves three well-posed problems at each iteration k :

- Solve the direct problem (1) to calculate the criterion (10).
- Solve the adjoint problem (18) to obtain an accurate estimation of the gradient of the criterion (20).
- Solve the sensitivity problem (12) to determine the descent step size in the direction of descent (13).

• **The sensitivity problem:** The variation of the unknown parameters is given by: $\boldsymbol{\tau}^+ = \boldsymbol{\tau} + \varepsilon\delta\boldsymbol{\tau}$. This results in the subsequent variation:

$$\begin{aligned}\varrho_i^+(t) &= \varrho_i(t) + \sum_{j=1}^{2n_i}\left(\varepsilon\delta\boldsymbol{\tau}_j^i\frac{\mathrm{d}\,\varrho_i}{\mathrm{d}\,\boldsymbol{\tau}_j^i}\right),\\ &= \varrho_i(t) + \varepsilon\sum_{j=1}^{2n_i}\left(\delta\boldsymbol{\tau}_j^i\frac{1}{\pi}\frac{\eta(-1)^{j+1}}{\eta^2+\left(t-\boldsymbol{\tau}_j^i\right)^2}\right).\end{aligned}$$

The varied temperature $T^+(x,y,t)$ is then a solution of:

$$\begin{cases}\rho C\dfrac{\partial T^+(x,y,t)}{\partial t} - \lambda\Delta T^+(x,y,t) = \\ \qquad\qquad\dfrac{\left(\sum\limits_{i=1}^{n_{heat}}\psi_i\phi_i\varrho_i^+(t)\right) - 2h\left(T^+(x,y,t)-T_0\right)}{e},\\ T^+(x,y,0) = T_0, \quad (x,y)\in\Omega,\\ -\lambda\dfrac{\partial T^+(x,y,t)}{\partial\vec{n}} = 0, \quad (x,y,t)\in\Gamma\times\left[0,t_f\right],\end{cases} \tag{11}$$

Considering δT as the temperature variation induced by the unknown parameters, we obtain its defining equation by subtracting Eq. (11) from Eq. (1). Consequently, δTsatisfies the resulting system:

$$\begin{cases}\rho C\dfrac{\partial\delta T(x,y,t)}{\partial t} - \lambda\Delta\delta T(x,y,t) = \\ \qquad\qquad\dfrac{\left(\sum\limits_{i=1}^{n_{heat}}\left(\dfrac{\psi_i\phi_i\eta}{\pi}\sum\limits_{j=1}^{2n_i}\left(\dfrac{(-1)^{j+1}\delta\boldsymbol{\tau}_j^i}{\eta^2+\left(t-\boldsymbol{\tau}_j^i\right)^2}\right)\right)\right) - 2h\delta T}{e},\\ \delta T(x,y,0) = 0, \quad (x,y)\in\Omega,\\ -\lambda\dfrac{\partial\delta T(x,y,t)}{\partial\vec{n}} = 0, \quad (x,y,t)\in\Gamma\times\left[0,t_f\right],\end{cases} \tag{12}$$

During each iteration, the descent depth is determined to minimize the criterion along the descent direction $\boldsymbol{d}^{k+1}$:

$$\gamma^{k+1} = \underset{\gamma^k \in \mathbb{R}^2}{\arg\min}\ J\left(\boldsymbol{\tau}^k - \gamma d^{k+1}\right) = \frac{\sum_{i=1}^{4}\int_0^{t_f}\left(T\left(C_i,t;\boldsymbol{\tau}^k\right)-\hat{T}_i(t)\right)\delta T\left(C_i,t;\boldsymbol{\tau}^k\right)dt}{\sum_{i=1}^{4}\int_0^{t_f}\left(\delta T\left(C_i,t;\boldsymbol{\tau}^k\right)\right)^2 dt}. \tag{13}$$

The descent direction is determined by the cost-function gradient and is defined by the conjugate gradient algorithm.

- **The adjoint problem:** The purpose of this problem is to determine the gradient of the cost-function: $\nabla J^k = \left(\frac{\partial J^k}{\partial \boldsymbol{\tau}_j^i}\right)_{\substack{i=1,\dots,n_{\text{heat}}\\ j=1,\dots,2n_i}}$. In order to accomplish this, we present the Lagrangian multipliers $Y(x,y,t)$ and the Lagrangian:

$$\mathfrak{L}(T,\boldsymbol{\tau},Y) = J(\boldsymbol{\tau}) + \iint_{\Omega\times[0,t_f]}\left(\rho C\frac{\partial T}{\partial t} - \lambda\Delta T - \frac{\mathrm{q}-2h(T-T_0)}{e}\right)Y\,d\Omega\,dt. \tag{14}$$

The variation of the Lagrangian is:

$$\delta\mathfrak{L}(T,\boldsymbol{\tau},Y) = \frac{\partial\mathfrak{L}}{\partial T}\delta T + \frac{\partial\mathfrak{L}}{\partial\boldsymbol{\tau}}\delta\boldsymbol{\tau} + \frac{\partial\mathfrak{L}}{\partial Y}\delta Y = \frac{\partial\mathfrak{L}}{\partial T}\delta T + \sum_{i=1}^{n_{\text{heat}}}\left(\sum_{j=1}^{2n_i}\left(\frac{\partial\mathfrak{L}}{\partial\boldsymbol{\tau}_j^i}\delta\boldsymbol{\tau}_j^i\right)\right) + \frac{\partial\mathfrak{L}}{\partial Y}\delta Y. \tag{15}$$

The Lagrange multiplier Y is fixed in order to satisfy following equation: $\frac{\partial\mathfrak{L}}{\partial T}\delta T = 0$. In addition, since the temperature T is a solution of (1), then $\delta J(\boldsymbol{\tau}) = \delta\mathfrak{L}(T,\boldsymbol{\tau},Y)$. In order to determine $Y(x,y,t)$, it is necessary to develop Eq. (15) from (14). The latter includes several terms:

$$\frac{\partial\mathfrak{L}}{\partial T}\delta T = \iint_{\Omega\times[0,t_f]}\left(\sum_{i=1}^{4}\left(T\left(C_i,t\right)-\hat{T}_i(t)\right)\delta T D_i\right)d\Omega\,dt + \rho C\iint_{\Omega\times[0,t_f]}\frac{\partial\delta T}{\partial t}Y\,d\Omega\,dt + \iint_{\Omega\times[0,t_f]}\left(-\lambda\Delta\delta T + \frac{2h}{e}\delta T\right)Y\,d\Omega\,dt. \tag{16}$$

In Eq. (16), the term D_i represents the Dirac distribution, which is used for punctual discrete measurements at sensors locations C_i. Thus, we can decompose (15) as follows:

$$\delta\mathfrak{L}(T,\boldsymbol{\tau},Y) = \iint_{\Omega\times[0,t_f]}E\ \ dxdydt + \rho C\ \delta\mathfrak{L}_1 + \delta\mathfrak{L}_2 + \sum_{i=1}^{n_{\text{heat}}}\left(\sum_{j=1}^{2n_i}\left(\frac{\partial\mathfrak{L}}{\partial\boldsymbol{\tau}_j^i}\delta\boldsymbol{\tau}_j^i\right)\right). \tag{17}$$

where:

$$E(x,y,t) = \sum_{i=1}^{4}\left(T\left(C_i,t\right)-\hat{T}_i(t)\right)\delta T D_i.$$

$$\delta\mathfrak{L}_1(x,y,t) = \iint_{\Omega\times[0,t_f]}\frac{\partial\delta T(x,y,t)}{\partial t}Y(x,y,t)\ dxdydt.$$

$$\delta\mathfrak{L}_2(x,y,t) = \iint_{\Omega\times[0,t_f]}\left(-\lambda\Delta\delta T(x,y,t) + \frac{2h}{e}\delta T(x,y,t)\right)Y\ dxdydt.$$

Several integrations by parts, the use of Green's theorem as well as the formulation of the sensitivity problem allow to simplify:

$$\delta\mathfrak{L}_1 = \int_\Omega\delta T(x,y,t_f)Y(x,y,t_f)\ dxdy - \iint_{\Gamma\times[0,t_f]}\delta T\frac{\partial Y}{\partial t}\ dxdydt.$$

$$\delta\mathfrak{L}_2 = -\iint_{\Omega\times[0,t_f]}\lambda\Delta(Y)\,\delta T\ dxdydt + \iint_{\Gamma\times[0,t_f]}\lambda\delta T\frac{\partial Y}{\partial\vec{n}}\ dxdydt + \iint_{\Omega\times[0,t_f]}\frac{2h}{e}\delta TY\ dxdydt.$$

As Y is fixed so that $\frac{\partial\mathfrak{L}}{\partial T}\delta T = 0$, then Y is solution of the following system (adjoint problem):

$$\begin{cases}\rho C\dfrac{\partial Y(x,y,t)}{\partial t} + \lambda\Delta Y(x,y,t) = E(x,y,t) + \dfrac{2h}{e}Y(x,y,t),\\ Y(x,y,t_f) = 0, \qquad (x,y)\in\Omega\\ -\lambda\dfrac{\partial Y(x,y,t)}{\partial\vec{n}} = 0, \qquad (x,y,t)\in\Gamma\times\left[0,t_f\right].\end{cases} \tag{18}$$

If Y is a solution of the adjoint problem described by the PDEs (18) while T is a solution of the direct problem described by the PDEs (1), Eq. (15) becomes:

$$\delta\mathfrak{L}(\theta,\boldsymbol{\tau},Y) = \sum_{i=1}^{n_{\text{heat}}}\left(\sum_{j=1}^{2n_i}\left(\frac{\partial\mathfrak{L}}{\partial\boldsymbol{\tau}_j^i}\delta\boldsymbol{\tau}_j^i\right)\right).$$

In addition, as $\delta J(\boldsymbol{\tau}) = \delta\mathfrak{L}(\theta,\boldsymbol{\tau},Y)$ and:

$$\frac{\partial\mathfrak{L}}{\partial\boldsymbol{\tau}_j^i}\delta\boldsymbol{\tau}_j^i = \iint_{\Omega\times T}\left(\frac{f_i g_i\eta}{\pi e}\left(\frac{(-1)^j\delta\boldsymbol{\tau}_j^i}{\eta^2+\left(t-\boldsymbol{\tau}_j^i\right)^2}\right)\right)Y\ dxdydt, \tag{19}$$

the expression of the gradient is then:

$$\frac{\partial J}{\partial\boldsymbol{\tau}_j^i} = \iint_{\Omega\times T}\left(\frac{f_i g_i\eta}{\pi e}\left(\frac{(-1)^j}{\eta^2+\left(t-\boldsymbol{\tau}_j^i\right)^2}\right)\right)Y\ dxdydt. \tag{20}$$

3.2.2. Identification strategy and algorithm

In [14], we demonstrated the effectiveness and accuracy of the CGM in offline situations. However, it should be noted that the identification of failure instants required around 10 min for a single simulation. One of the main drawbacks of this offline identification is its convergence time, which can be significantly longer depending on the complexity of the problem. To address this challenge and improve identification time, we propose a quasi-online identification strategy. In the following, the notations below are considered:

- $\mathcal{T}_i = [t_i, t_{i+1}] \subset [0, t_f]$ is the current time interval, corresponding to the time during which the process evolves. Its state (temperature) is the solution of the direct problem (1) over the time interval $\mathcal{T}_i$.
- $\mathcal{T}_i^* = [t_i^*, t_{i+1}^*]$ is the time interval used to solve the inverse problem.
- t_{detect} is the time instant at which the failure is initially detected by the EWMA control chart. It serves as the starting point for launching the subsequent identification process.
- t_{diag} is the time instant when comprehensive diagnostic information becomes available. It is calculated as the sum of t_{detect} and the time taken for the identification process to converge. Mathematically, it can be expressed as $t_{\text{diag}} = t_{\text{detect}}$+Convergence Time.

To illustrate the quasi-online identification phase for thermal source failures, let us take the example where the mobile source q_1 fails at time $t = 1500$s. Once the failure is detected, i.e. when the limits of the EWMA map are exceeded (Fig. 7), the identification procedure is launched. In this identification, the window used is defined as $\mathcal{T}_i^* = [t_i - \nu, t_{i+1}]$. This adapted window improves the accuracy of identifying source failure or restart times. Indeed, by subtracting the value of ν from the identification window, we obtain a longer period over which the measurements are taken into account, resulting in a more accurate estimate of source failure or restart instants.

The choice of the ν value in the identification window depends on the level of noise present in the sensor measurements. High noise levels lead to late detection. It is therefore possible to adjust the value of ν appropriately. By increasing the value of ν, the identification window is extended over a longer period of time, so that failure-induced variations can be better taken into account.

Finally, an adaptation of the conjugate gradient algorithm is presented in the algorithm 1 . The algorithm stops when the criterion (10) is judged sufficiently small. Details of the stopping criterion are given in the next section.

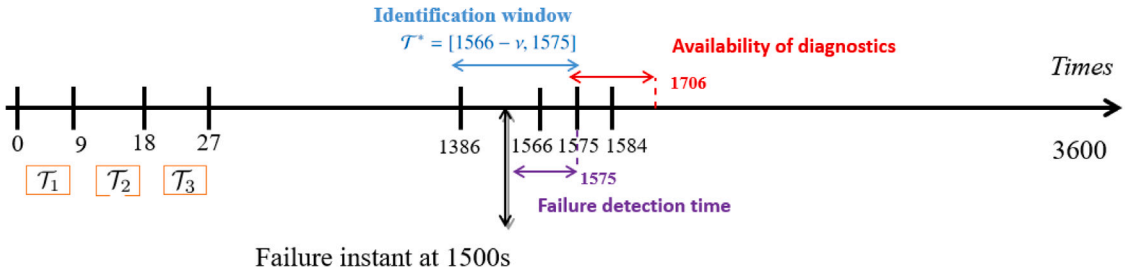

Fig. 9. Overview of the quasi-online diagnostic method: integrating real-time detection and quasi-online identification.

Algorithm 1 CGM quasi-online algorithm.

1. Compute the EWMA statistic $Z_{i,m}$ over the time interval $\mathcal{T}_i$.
2. Evaluate the EWMA UCL and LCL:
   (a) If the limits are not exceeded, it implies that no failure has occurred within the interval $\mathcal{T}_i$. Terminate the detection procedure and proceed to the next time interval $\mathcal{T}_{i+1}$ (go to step 1 with $i = i + 1$).
   (b) If the EWMA control limits are exceeded, this means that a failure has occurred over this $\mathcal{T}_i$ window. An identification procedure is performed on $\mathcal{T}_i^* = [t_i - v, t_{i+1}]$:
      i. choose an initialization $\boldsymbol{\tau}^k$ for iteration $k = 0$ for switching instants.
      ii. Solve the adjoint problem over the time interval $\mathcal{T}_i^*$.
      iii. calculation of the direction of descent over the interval $\mathcal{T}_i^*$ considering the gradient of the cost function resulting from the previous solutions of the adjoint problem.
      iv. Solve the sensitivity problem over the time interval $\mathcal{T}_i^*$ to calculate the depth of descent (in the direction of descent).
      v. Update unknown parameter $\boldsymbol{\tau}^{k+1} = \boldsymbol{\tau}^k - \gamma^{k+1}\boldsymbol{d}^{k+1}$ over time interval $\mathcal{T}_i^*$. (return to step 1 with $i = i + 1$).

3.2.3. Example

Considering the illustrative context where the identification of the failure of source q_1 has to be performed from the observations obtained in Fig. 6. In this section, the measurements collected from the four sensors data are treated with an uncertainty characterized by zero-mean Gaussian noise and distinct standard deviations σ. In order to implement the CGM algorithm, a J_{stop} threshold must be defined. The stopping criterion to stop the iterative minimization of the criterion is chosen according to the criterion proposed by [28,32]:

$$J_{\text{stop}} = \Delta t \; N_c \; N_t \; \sigma^2, \tag{21}$$

where $N_c = 4$ is the number of sensors, N_t is the number of measurements data collected by sensors during the identification interval $\mathcal{T}^*$, $\Delta t = 9$ s is the time sampling step between each measurement and σ^2 is the variance of the Gaussian measurement noise. On a personal computer with the following characteristics, numerical results are achieved using the Comsol-Multiphysics solver interfaced with Matlab software: CPU: Intel® Core(TM) i5-10210U CPU 2.11 GHz, RAM: 8.00 Go, OS: Windows 10 (64).

In the previous analysis, we evaluated the effectiveness of the EWMA control chart, as described in Section 3.1. The chart identifies the time of failure detection as $t_{\text{detect}} = 1575$s. Subsequently, we launch the identification process, initializing the parameters $v = 180$s and $t^1_{\text{nok},1} = \frac{1575+1386}{2}$ seconds. Utilizing the stopping criterion (21), the process converged to a failure identification time of $t^1_{\text{nok},1} = 1502$ s within only 131 s. This implies that the diagnostic information becomes available $t_{\text{diag}} = t_{\text{detect}} + 131 = 1575 + 131 = 1706$ s. Fig. 10 illustrates how the cost function evolves with each iteration. This highlights the effectiveness of the proposed quasi-online identification strategy compared with the offline method, which required 10 min for a similar identification.

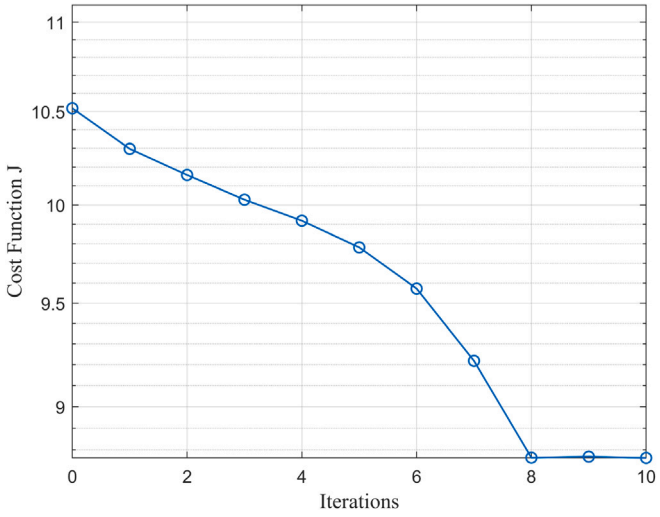

Fig. 10. Example of Criterion evolution in case $\sigma = 0.1$ °C.

Fig. 9 provides a comprehensive summary of this quasi-online diagnostic method, incorporating both real-time detection and quasi-online identification.

The Table 2 presents the identification results obtained by the CGM approach. On 30 simulations, the results are presented as the mean and standard deviation (in brackets), where $t^1_{\text{nok},1}$, t_{detect} and t_{diag} represent the identification result, detection and diagnosis times respectively. The approach performs very effectively in scenarios with low measurement noise, and maintains high accuracy even in the presence of high measurement noise.

Following the presentation and analysis of the first approach, it is essential to emphasize its significance. In the subsequent section, we introduce a second method based on the Bayesian filter, which builds upon our recent work [33,34]. This alternative approach serves to further enhance our understanding and broaden the scope of our investigation.

3.3. Failure identification by the Bayesian filter

3.3.1. State estimation problem

State estimation inverse problems are highly relevant in practical applications [19,35,36]. These problems involve the estimation of dynamic variables using observable data and prior knowledge of physical

Table 2
Quasi-online identification of q_1 heat source failure instants by CGM method, with varying noise levels.

		Real failure	Identification result $t^1_{nok,1}$	Detection instant t_{detect}	Availability of diagnostics t_{diag}
$\sigma = 0.1$ °C	CGM	1500 s	1501.8 s (1.64)	1575 s (0.87)	1645.7 s (5.95)
$\sigma = 0.5$ °C	CGM	1500 s	1502.7 s (2.19)	1611 s (0.60)	1696.9 s (13.4)
$\sigma = 1$ °C	CGM	1500 s	1503.2 s (2.59)	1629.5 s (1.35)	1714.3 s (21.4)

processes. They are typically addressed through Bayesian filters. The Kalman filter is the most widely used Bayesian filter method, particularly for linear models with additive Gaussian noises. In order to address the evolution and observation problems within this framework, it is necessary to redefine the direct problem (1). A numerical approach utilizing the finite difference method is proposed for this task [37]. The discretization of the system (1) using finite differences and the construction of the evolution and observation models are explicitly demonstrated and analyzed in [33]. Consequently, the application can be formulated as follows:

$$\begin{cases} \boldsymbol{T}^{k+1} = \boldsymbol{L} \cdot \boldsymbol{T}^k + \boldsymbol{B}^k \cdot \boldsymbol{G}^k + \boldsymbol{H}, \\ \boldsymbol{T}^k_{\boldsymbol{obs}} = \boldsymbol{C} \cdot \boldsymbol{T}^k, \end{cases} \tag{22}$$

where $\boldsymbol{T}^k$ is a matrix containing temperature of all discretized points of the plate at the instant k, $\boldsymbol{L}$ is the transition matrix, encodes the linear combination of $\boldsymbol{T}^k$, that connects state k to state $k+1$, the matrix $\boldsymbol{B}^k$ encodes the coordinates of the Gaussian distribution surrounding the point (x_i, y_i) based on the mobile source's spatial support ψ_i^k. The heat flux ϕ_i^k $i = 1, \ldots, 3$, is encoded by the matrix $\boldsymbol{G}^k$, and the position of the fixed sensors is encoded by the matrix $\boldsymbol{C}$. Finally, $\boldsymbol{H}$ is a constant vector that depends on discretization and model parameters.

3.3.2. The Bayesian filter

With the assumption that both the evolution and observation models defined in system (22) are linear, the Kalman filter was used. In such models, it is assumed that the noises are Gaussian with known means and covariances, and that they are additive. The system (22) is then modified as follows:

$$\begin{cases} \boldsymbol{T}^{k+1} = \boldsymbol{L} \cdot \boldsymbol{T}^k + \boldsymbol{B}^k \cdot \boldsymbol{G}^k + \boldsymbol{H} + \boldsymbol{w}_k, \\ \boldsymbol{T}^k_{obs} = \boldsymbol{C} \cdot \boldsymbol{T}^k + \boldsymbol{v}_k, \end{cases} \tag{23}$$

where $\boldsymbol{w}_k$, $\boldsymbol{v}_k$ are the evolution and observation noises respectively with zero means and covariances matrices $\boldsymbol{Q}$ and $\boldsymbol{R}$ respectively. To estimate the input vector $\boldsymbol{G}^k$, a technique involves modifying the classical Kalman filter to incorporate the input vector into the state vector. By including the input vector, we can estimate the behavior of the heat flux ϕ_i^k for each source ($i = 1, \ldots, 3$). This estimation of the heat flux behavior provides valuable insights and aids in identifying potential failures in the heat sources. The evolution and observation models may be respectively expressed as follows:

$$\begin{cases} \boldsymbol{\Theta}^{k+1} = \mathcal{L}^k \cdot \boldsymbol{\Theta}^k + \boldsymbol{H}' + \boldsymbol{w}'_k, \\ \boldsymbol{T}^k_{obs} = \boldsymbol{C}' \cdot \boldsymbol{\Theta}^k + \boldsymbol{v}_k, \end{cases} \tag{24}$$

where:

$$\boldsymbol{\Theta}^{k+1} = \begin{bmatrix} \boldsymbol{T}^{k+1} \\ \boldsymbol{G}^{k+1} \end{bmatrix}, \quad \mathcal{L}^k = \begin{bmatrix} \boldsymbol{L} & \boldsymbol{B}^k \\ \boldsymbol{0} & \mathbf{I} \end{bmatrix} \quad \text{and} \quad \boldsymbol{C}' = \begin{bmatrix} \boldsymbol{C} & 0 \end{bmatrix}.$$

Fig. 11 shows the integrated procedure using the Kalman filter. Finally, after reformulating the system (23) into (24) with the integration of the input vector $\boldsymbol{G}$ into the state vector, we are ready to use the Kalman filter. The posteriori density is Gaussian and the Kalman filter gives the optimal solution to the state estimation problem. $\mathcal{L}^k$ and $\boldsymbol{C}'$ are given matrices for the corresponding state $\boldsymbol{\Theta}^k$ and observation $\boldsymbol{T}^k_{obs}$, also, $\boldsymbol{H}'$ is a constant vector for the model of the state evolution $\boldsymbol{\Theta}^k$, and $\mathbf{I}$ is the matrix identity.

In the following, $\boldsymbol{\Theta}$ is a Gaussian with calculable mean and covariance. We denote by $\boldsymbol{\mu}$ and $\boldsymbol{\Sigma}$ the means and covariance, respectively. Given that $\boldsymbol{Q}'$ and $\boldsymbol{R}$ are also Gaussian. Considering the noises, $\boldsymbol{w}'$ with zero mean multivariate normal distribution $\mathcal{N}$ and covariance matrix

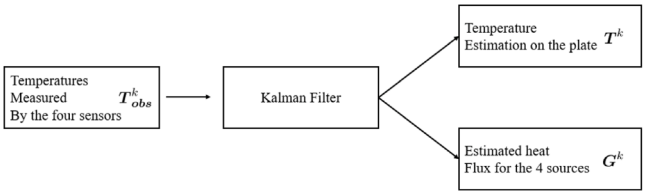

Fig. 11. Kalman filter schema.

$\boldsymbol{Q}'$: $\boldsymbol{w}' \sim \mathcal{N}(0, \boldsymbol{Q}')$, and $\boldsymbol{v}$ with a zero mean and covariance matrix $\boldsymbol{R}$: $\boldsymbol{v} \sim \mathcal{N}(0, \boldsymbol{R})$. The prediction and update steps of the Kalman filter, for each $k = 1, \ldots, t^*$, where $t^* = t_f / \Delta t_{obs}$, are given by Algorithm 2.

Algorithm 2 Kalman filter.

i. Initialize: $\hat{\boldsymbol{\mu}}_{0|0}$ and $\boldsymbol{\Sigma}_{0|0}$.
ii. For $k = 1, 2, ..., t^*$:

Prediction:

$$\hat{\boldsymbol{\mu}}_{k|k-1} = \mathcal{L}_k \hat{\boldsymbol{\mu}}_{k-1|k-1} + \boldsymbol{H}', \tag{25}$$

$$\hat{\boldsymbol{\Sigma}}_{k|k-1} = \mathcal{L}_k \hat{\boldsymbol{\Sigma}}_{k-1|k-1} {\mathcal{L}_k}^T + \boldsymbol{Q}. \tag{26}$$

Update:

$$\boldsymbol{K}_k = \hat{\boldsymbol{\Sigma}}_{k|k-1} {\boldsymbol{C}'}^T \left(\boldsymbol{C}' \hat{\boldsymbol{\Sigma}}_{k|k-1} {\boldsymbol{C}'}^T + \boldsymbol{R} \right)^{-1}, \tag{27}$$

$$\hat{\boldsymbol{\mu}}_{k|k} = \hat{\boldsymbol{\mu}}_{k|k-1} + \boldsymbol{K}_k \left(\boldsymbol{T}^k_{obs} - \boldsymbol{C}' \hat{\boldsymbol{\mu}}_{k|k-1} \right), \tag{28}$$

$$\hat{\boldsymbol{\Sigma}}_{k|k} = \left(\mathbf{I} - \boldsymbol{K}_k \boldsymbol{C}' \right) \hat{\boldsymbol{\Sigma}}_{k|k-1}. \tag{29}$$

The Kalman gain matrix is represented by $\boldsymbol{K}_k$ in this algorithm, $\boldsymbol{T}^k_{obs}$ is the observation vector at time k. In the application, temperatures are not measured at each time (they are only measured every 9 s), therefore if there is no measurement at time k, then $\hat{\boldsymbol{\mu}}_{k|k} = \hat{\boldsymbol{\mu}}_{k|k-1}$.

When a failure is detected by the EWMA control chart, the Kalman filter stops its real-time state estimation at time t_{detect}. This key moment marks the start of the Kalman smoothing algorithm [38,39], which performs inverse state estimation from $k = t^* = t_{detect}, \ldots, 1$. The hybrid approach takes advantage of the computational speed of the Kalman filter for online estimation and the accuracy of the Kalman smoother for offline analysis. For this algorithm, we assume that the Kalman filter has already been applied; the reverse steps are detailed in Algorithm 3.

Algorithm 3 Kalman Smoother.

i. Initialize: $\hat{\boldsymbol{\mu}}_{t^*|t^*}$, $\hat{\boldsymbol{\Sigma}}_{t^*|t^*}$.
ii. For $k = t^* - 1, t^* - 2, \cdots, 1$:

$$\boldsymbol{\mathcal{P}}_k = \hat{\boldsymbol{\Sigma}}_{k|k} \boldsymbol{L}_k^T \hat{\boldsymbol{\Sigma}}^{-1}_{k+1|k}.$$

$$\hat{\boldsymbol{\mu}}_{k|t^*} = \hat{\boldsymbol{\mu}}_{k|k} + \boldsymbol{\mathcal{P}}_k (\boldsymbol{\mu}_{k+1|t^*} - \hat{\boldsymbol{\mu}}_{k+1|k}).$$

$$\hat{\boldsymbol{\Sigma}}_{k|t^*} = \hat{\boldsymbol{\Sigma}}_{k|k} + \boldsymbol{\mathcal{P}}_k (\boldsymbol{\Sigma}_{k+1|t^*} - \hat{\boldsymbol{\Sigma}}_{k+1|k}) \boldsymbol{\mathcal{P}}_k^T.$$

Table 3
Quasi-online identification of q_1 heat source failure instants by KS method, with varying noise levels.

		Real failure	Identification result $t^1_{nok,1}$	Detection instant t_{detect}	Availability of diagnostics t_{diag}
$\sigma = 0.1$ °C	KS	1500 s	1506 s (0.608)	1566 s (0)	1641.5 s (3.6)
$\sigma = 0.5$ °C	KS	1500 s	1505.6 s (1.52)	1611.2 s (1.01)	1671.7 s (9.8)
$\sigma = 1$ °C	KS	1500 s	1504.9 s (2.82)	1629 s (1.52)	1688.4 s (16.37)

3.3.3. Estimation methodology

To estimate the failure and the restart times, an assumption was made that the failures of the sources are independent events, allowing them to be treated individually. Furthermore, the knowledge of the theoretical signal of each source without failure, denoted as ϕ_i^k and graphically represented in Fig. 2, was utilized. Given a set of candidate vectors ϱ_{cand}, the problem is to find the optimal candidate vector ϱ_{opt} that minimizes the squared error (SE) between $\phi_i^k \times \varrho_{cand}^i$ and $\widehat{\phi}_i^k$.

Mathematically, this can be expressed as follows:

$$\varrho^i_{\text{opt}} = \underset{\varrho_{cand}}{\text{Arg min}} \sum_{k}^{t^*} \left(\phi_i^k \times \varrho^i_{cand} - \widehat{\phi}_i^k \right)^2, \tag{30}$$

where ϱ^i_{cand} represents the candidate vector which corresponds to source i, ϕ_i^k is the theoretical signal of each source without failure, and $\widehat{\phi}_i^k$ is the estimated flux of ϕ_i^k. Thus, for each source, the following algorithm 4 can be used:

Algorithm 4 Search strategy algorithm.

i. Initialize and define the bounds of the candidate vector ϱ^i_{cand}.
ii. Compute the squared error (SE) between $\phi_i(t) \times \varrho^i_{cand}$ and $\widehat{\phi}_i(t)$.
iii. Solve problem (30) by performing an iterative search to find the value of ϱ^i_{cand} that minimizes the squared error, while respecting the constraints defined by the bounds.
iv. Return the optimal value of ϱ^i_{opt} that minimizes the squared error, along with the minimum value of the squared error.

3.3.4. Example

For the purpose of demonstrating the proposed methodology, let us consider the previous illustrative context where the first source q_1 fails at $t = 1500$ s. Parameters are given in the following Table 4 and the evolution of the temperatures at the four sensors are shown in Fig. 6, similar to the previous analysis, the measurement data are treated with an uncertainty characterized by zero-mean Gaussian noise and distinct standard deviations σ.

The results are given in Table 3 with different noise levels. It is important to note that in the case of late detection, this second approach based on KS produces more accurate identification results. Indeed, the principle of KF is to use past observations to improve future estimates. So, when a failure detection is late, the filter has more observations to estimate the heat flux, which can lead to more accurate identification of failure instants. In other terms, the more data available to the KF, the more accurate the estimates.

In the following section, we explore different configurations to present the implementation of the Conjugate Gradient Method (CGM) and compare it to the second approach based on Kalman smoother (KS). Through this in-depth evaluation, we aim to provide a comprehensive assessment that highlights both the advantages and disadvantages of our recent approach.

4. Numerical results

In this section, several scenarios have been simulated in order to illustrate the appropriateness of the proposed approaches. Starting by preventing the inverse crime, data have been collected from a Comsol-Multiphysics simulation with different parameters: time step $\Delta t = 1$ s and space step $\Delta x = \Delta y = 0.01$ m. Matlab has been used to analyze this data.

Table 4
Mathematical model parameters.

Symbol	Definition	Values
ρC	Volumetric heat	$2.421.10^6$ J m^{-3} K^{-1}
h	Natural convection coefficient	10 W m^{-2} K^{-1}
λ	Thermal conductivity	178 W m^{-1} K^{-1}
θ_0	Initial temperature	293 K
t_f	Final time	3600 s
e	Thickness	$2 \cdot 10^{-3}$ m
Δt	Time step	3 s
Δt_{obs}	Time step of the observations	9 s
$\Delta x, \Delta y$	Space step	0.05m

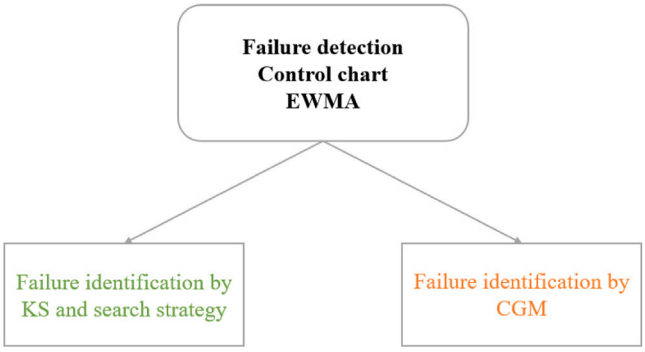

Fig. 12. Illustration of failure detection followed by identification using both approaches.

Building on the previous section's description and analysis of the quasi-online diagnostic approach, which integrates real-time fault detection via the EWMA control chart and an identification process based on two distinct methodologies, Fig. 12 illustrates this integrated diagnostic process. The four sensors' data uncertainty is represented by a Gaussian noise with a zero mean and different σ standard deviations, similarly to a real system.

To fully understand the effect of this factor, the obtained results are presented in a manner similar to the preceding section, based on 30 simulations for each scenario.

4.1. Source separation: 3 heat sources with same failure instant

In the next phase of our study, we extend our focus from identifying the failure instants of a single source to a more complex scenario involving several sources. More precisely, we aim to identify the failure instants of three distinct heat sources. In this multi-source framework, all three sources q_1, q_2 and q_3 are assumed to fail simultaneously at t=1500 s. This complexity makes it even more difficult to accurately identify individual failure sources, especially when they fail simultaneously. The aim is to evaluate the ability of our two diagnostic approaches to accurately differentiate and identify the failure instants of these sources under such complex conditions (see Fig. 13).

Table 5 shows the identification results obtained by the two approaches for 30 simulations, where $t^1_{nok,1}$, $t^2_{nok,1}$, and $t^3_{nok,1}$ represent

Table 5
Quasi-online identification of q_1, q_2 and q_3 heat sources failure instants by CGM and KS methods, with varying noise levels.

		Identification result	Detection instant t_{detect}	Availability of diagnostics t_{diag}
$\sigma = 0.1$ °C	CGM	$t^1_{nok,1} = 1504.8$ s (2.74) $t^2_{nok,1} = 1499.1$ s (2.64) $t^3_{nok,1} = 1490.3$ s (5.88)	1562.9 s (2.11)	1648.1 s (9.6)
	KS	$t^1_{nok,1} = 1505.2$ s (1.32) $t^2_{nok,1} = 1497.8$ s (1.63) $t^3_{nok,1} = 1586.4$ s (6.22)	1563.4 s (1.69)	1631.3 s (5.75)
$\sigma = 0.5$ °C	CGM	$t^1_{nok,1} = 1503.1$ s (3.25) $t^2_{nok,1} = 1499.8$ s (4.17) $t^3_{nok,1} = 1494.1$ s (4.07)	1574 s (4.04)	1669.9 s (15.4)
	KS	$t^1_{nok,1} = 1505.3$ s (4.82) $t^2_{nok,1} = 1497.3$ s (7.30) $t^3_{nok,1} = 1578$ s (5.35)	1575.3 s (1.57)	1639.1 s (7.47)
$\sigma = 1$ °C	CGM	$t^1_{nok,1} = 1501.8$ s (4.31) $t^2_{nok,1} = 1500.5$ s (5.64) $t^3_{nok,1} = 1496.3$ s (7.98)	1585.8 s (6.42)	1702.3 s (21.4)
	KS	$t^1_{nok,1} = 1505.1$ s (9.4) $t^2_{nok,1} = 1506.2$ s (8.3) $t^3_{nok,1} = 1576.8$ s (6.98)	1585.8 s (2.1)	1646.4 s (7.4)

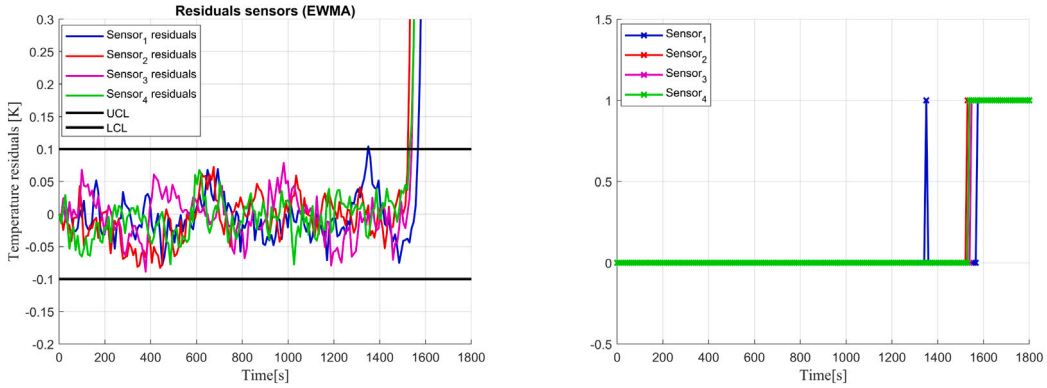

(a) EWMA control chart based on residues: online detection phase.

(b) Decision chart.

Fig. 13. Illustration of online detection of three heat sources q_1, q_2 and q_3 using the parameters: $\zeta = 0.2$ and $\sigma = 0.1$ °C.

the identification result, t_{detect} and t_{diag} represent detection time and diagnosis time respectively.

Under conditions of low measurement noise, both the CGM and KS methods demonstrate excellent efficiency in identifying sources q_1 and q_2. However, when it comes to the q_3 source, the CGM method clearly outperforms the KS method. This better performance of the CGM method is largely due to its better handling of the sensor's delay in responding to changes from this more distant source, which intrinsically complicates the identification process. In situations where measurement noise levels are higher, the CGM method continues to display a higher degree of identification accuracy than the KS method. This is particularly evident in scenarios involving late failure detection, where the CGM method's ability to make effective use of a larger volume of observation data significantly improves the accuracy of identifying the exact time of failure.

4.2. Source separation: 2 heat sources with different failure instants

Following the successful identification of simultaneous failures of three separate heat sources, the focus now shifts to a more complex scenario: the identification of non-simultaneous failures of two separate sources. In this specific configuration, the initial source fails at $t^1_{nok,1} = 1000$ s, while the second source fails later, precisely $t^2_{nok,1} = 2000$ s after the start of the simulation.

When a failure is detected by the control chart, the system proceeds to the identification phase to specify the failed heat source (Figs. 14(a), 14(b)). The results of this identification are shown in Table 6. Having identified the failure time of the first heat source, a direct problem is solved using this identification, with the aim of updating the system behavior according to the new observations. The time required for this update is called Δ_t^{Res}. Once this update is complete, the detection phase is reset and reactivated (Figs. 14(c), 14(d)). Once the second failure has been identified, the availability of the next diagnosis is given by $t_{diag} = t_{detect} +$ convergence time $+ \Delta_t^{Res}$.

Table 6 shows the results of failure identification using two different methods over 30 simulations. In situations where the measurement noise is low, both methods were remarkably effective in identifying failures. However, in scenarios characterized by high measurement noise, the CGM approach notably outperformed the KS method in terms of accuracy. Furthermore, in line with previous results, the proposed GCM-based approach gave solid results for failure identification in cases of late detection. This improved performance can be attributed to the increased number of observations available during late detection phases, which contributes significantly to more accurate fault identification. This comparison underlines the superior adaptability and efficiency of the CGM method, particularly under difficult high-noise conditions.

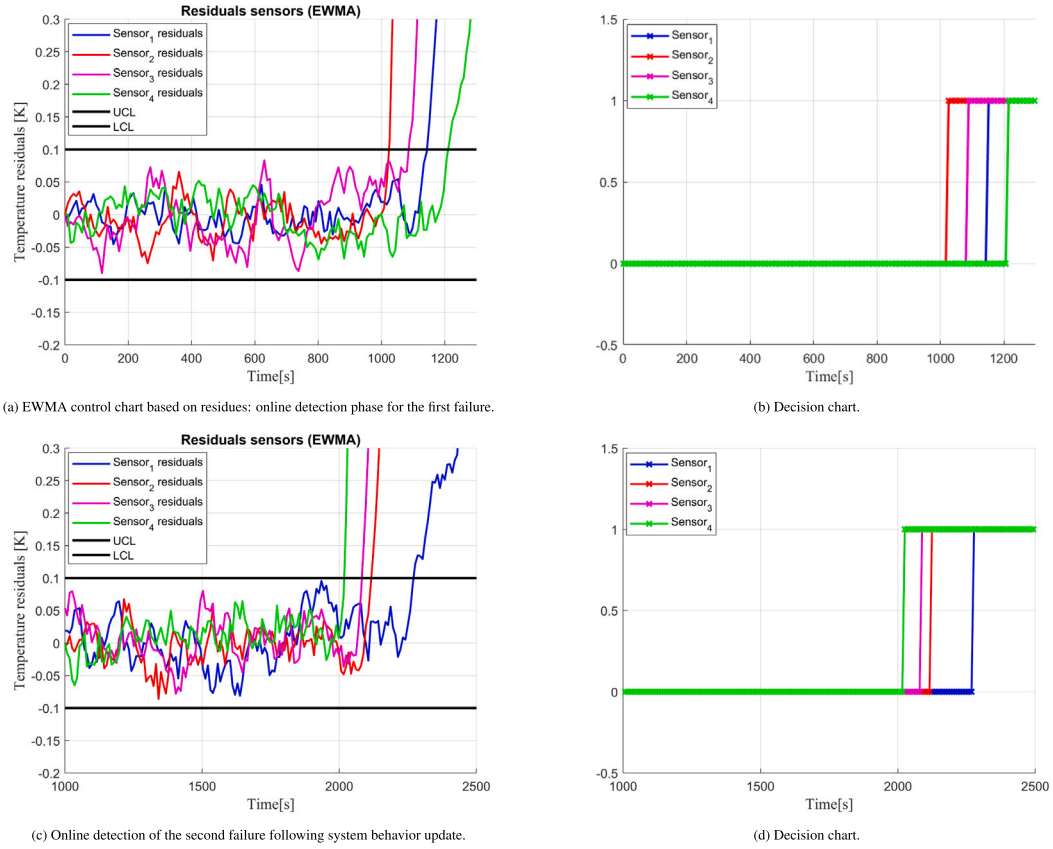

(a) EWMA control chart based on residues: online detection phase for the first failure.

(b) Decision chart.

(c) Online detection of the second failure following system behavior update.

(d) Decision chart.

Fig. 14. Illustration of online failure detection for two heat sources q_1 and q_2 using the parameters: $\zeta = 0.2$ and $\sigma = 0.1$ °C.

Table 6
Quasi-online identification of q_1 and q_2 heat sources failure instants by CGM and KS methods, with varying noise levels.

		Identification result $t^1_{nok,1}$	t_{detect} and t_{diag}	Identification result $t^2_{nok,1}$	t_{detect} and t_{diag}
$\sigma = 0.1$ °C	MGC	1003.9 s (1.36)	1154.3 s(0.96) 1203.9 s(10.77)	2001.6 s (1.79)	2119.5 s(1.19) 2228.4 s(12.2)
	KS	1015.7 s (2.88)	1147 s(2.23) 1191.7 s (11.24)	2003.9 s (0.71)	2135.2 s(0.44) 2211.9 s (4.7)
$\sigma = 0.5$ °C	MGC	1004.2 s (3.64)	1206 s(2.27) 1271.8 s (25.7)	1999.1 s (2.1)	2175.8 s(1.91) 2301.1 s (22.07)
	KS	1008.6 s (4.5)	1211 s(1.84) 1257.5 s (16.28)	2004 s (2.52)	2182.2 s(1.2) 2277.8 s (12.4)
$\sigma = 1$ °C	MGC	1004.7 s (3.28)	1240.6 s (3.19) 1336.6 s (31.77)	1999.3 s (3.71)	2221.1 s(4.1) 2348 s (31.1)
	KS	1007.3 s (8.99)	1242 s(3.29) 1290 s (30.33)	2005.1 s (5.3)	2228.8 s(3.52) 2329.8 s (34.54)

Table 7
Quasi-online identification of q_2 and q_3 heat sources failure instants and restart for q_2 by CGM and KS methods, with varying noise levels.

		$t^2_{nok,1}$	t_{detect} and t_{diag}	$t^3_{nok,1}$	t_{detect} and t_{diag}	$t^2_{ok,1}$	t_{detect} and t_{diag}
$\sigma = 0.1$ °C	CGM	1001.5 s (3.1)	1165 s(2.01) 1257.6 s(11.8)	1503.3 s (2.08)	1610.9 s(2.6) 1659 s(7.02)	2505.6 s (7.97)	2808.4 s(2.3) 2903 s(13.4)
	KS	1007.2 s (2.3)	1165.8 s(1.45) 1209.5 s (14.32)	1507.4 s (1.96)	1611.1 s(3.2) 1651.7 s (5.6)	2512.4 s (7.01)	2799.2 s(3.48) 2910.3 s(3.2)
$\sigma = 0.5$ °C	CGM	1001.3 s (4.84)	1244 s(2.03) 1281.4 s (32.14)	1505.2 s (6.55)	1665.1 s(2.63) 1744.4 s (14.76)	2504.1 s (10.4)	2934.3 s(5.91) 3046.3 s(22.2)
	KS	1004.7 s (13.8)	1244.5 s(2.18) 1290.3 s (20.4)	1508.4 s (5.31)	1656 s(1.15) 1721.6 s (10.7)	2535 s (9.79)	2925 s(8.5) 3033.8 s(10.1)
$\sigma = 1$ °C	CGM	1001.2 s (5.28)	1276.6 s (3.19) 1336.6 s (31.77)	1504.8 s (3.71)	1692.1 s(2.1) 1772 s (29.7)	2504.6 s (12.7)	3123.5 s(1.19) 2228.4 s(12.2)
	KS	1004.3 s (8.9)	1277.7 s(2.85) 1330.6 s (25.33)	1508.8 s (8.6)	1691.8 s(2.15) 1751.7 s (22.34)	2522.6 s (10.2)	3106 s(1.19) 3278.4 s(12.2)

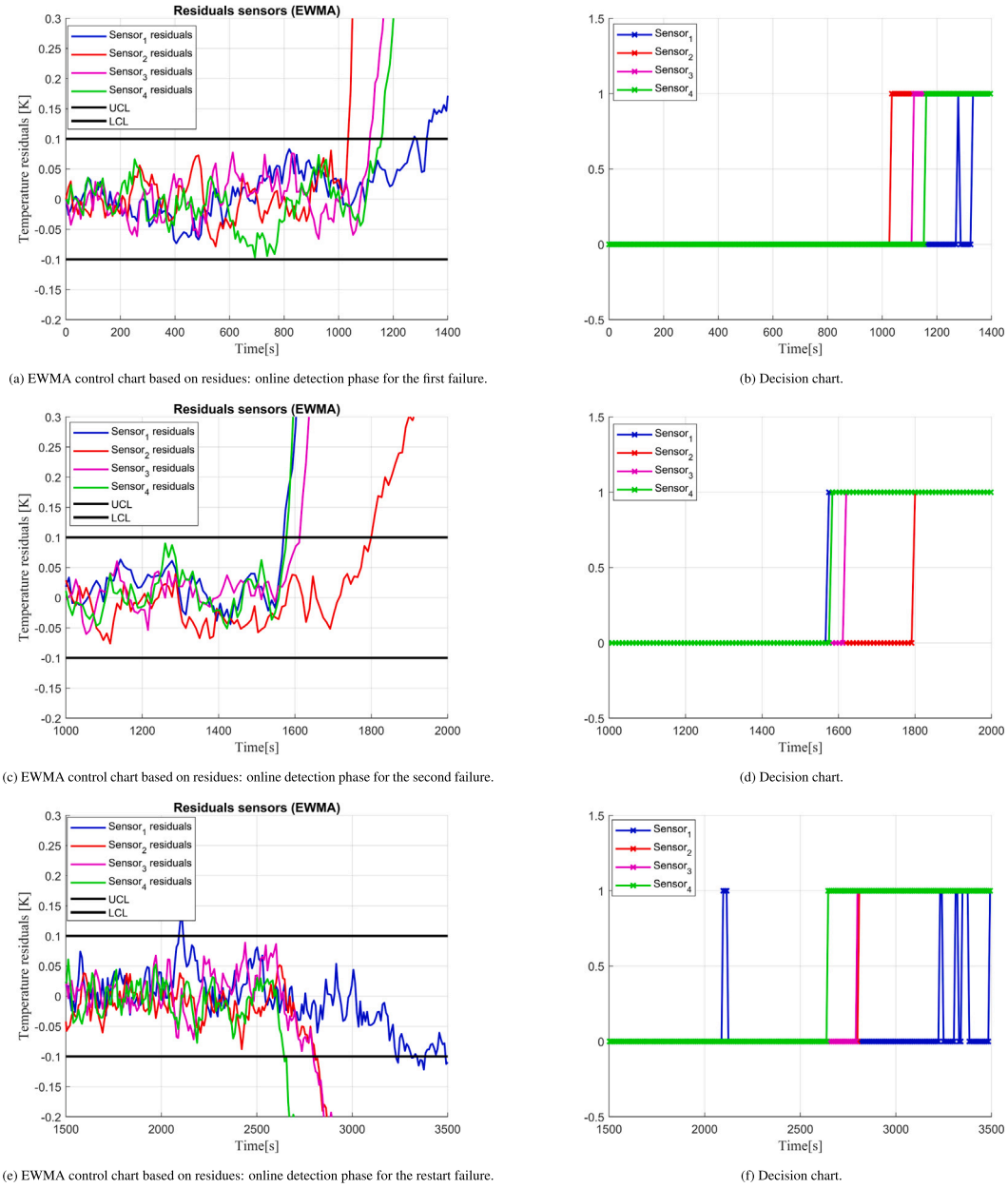

(a) EWMA control chart based on residues: online detection phase for the first failure.

(b) Decision chart.

(c) EWMA control chart based on residues: online detection phase for the second failure.

(d) Decision chart.

(e) EWMA control chart based on residues: online detection phase for the restart failure.

(f) Decision chart.

Fig. 15. Illustration of online failure detection for two heat sources q_2, q_3 and restart for q_2 using the parameters: $\zeta = 0.2$ and $\sigma = 0.1$ °C.

4.3. Identifying of failure and restart instants

After successfully identifying failure cases for two distinct sources using both approaches, we extend the challenge of identifying failure instants alone to also include source restart instants. In this advanced scenario, we focus on two distinct heat sources with more complex behaviors. Specifically, we are considering a situation in which the second heat source q_2 fails at $t^2_{\text{nok},1} = 1000$ s then restarts at $t^2_{ok,1} = 2500$ s. At the same time, the third heat source q_3 fails at $t^3_{\text{nok},1} = 1500$s. The aim of this new complexity is to evaluate the adaptability and accuracy of our two diagnostic approaches in identifying not only failures, but also restarts of the heat sources.

As explained in the previous configuration, once the first failure has been detected and identified (Figs. 15(a), 15(b)), we proceed to solve a "direct problem" using the identification results. This step serves to reconfigure the system's behavior based on the identified failure times. The time allocated to this process is denoted as $\Delta_t^{Res_1}$. Once this update has been carried out, the detection mechanism is reset and restarted (Figs. 15(c), 15(d)). When a new failure is identified, the availability of the next diagnostic step is determined by the equation $t_{\text{diag}} = t_{\text{detect}} +$ convergence time $+ \Delta_t^{Res_1}$.

Finally, when both failures have been identified and the system's behavior updated accordingly (requiring an additional $\Delta_t^{Res_2}$ time), we reset the detection process once again (Figs. 15(e), 15(f)). The system then proceeds on to the identification phase, this time with the specific aim of identifying instants of restarting failed heat sources. The time taken to provide the next diagnostic data after restart identification is calculated as follows: $t_{\text{diag}} = t_{\text{detect}} +$ convergence time $+ \Delta_t^{Res_1} + \Delta_t^{Res_1}$.

Table 7 compares the performance of the CGM and KS approaches in identifying failure and restart instances. In conditions where measurement noise is relatively low, both methods give satisfactory results. However, in situations where measurement noise is high, the CGM approach clearly outperforms the KS method, demonstrating greater accuracy in identifying failure and restart times. This comparison highlights the superior performance of the CGM method, particularly in environments with high noise levels. Overall, the table reinforces the

effectiveness of our CGM method in accurately identifying these critical moments, particularly in contexts involving systems governed by parabolic partial differential equations.

5. Conclusion

In this article, we introduced a quasi-online methodology designed to identify failure instants within a physical system governed by a set of linear parabolic partial differential equations. Our objective was to determine when and which mobile heat source had experienced a failure or restart based on noisy temperature observations from four fixed sensors.

The quasi-online diagnosis process consists of two key phases: detection and identification. For real-time failure detection, we employed the EWMA control chart, which effectively detects failures when one or more heat sources malfunction, subsequently triggering the identification process. In this identification phase, we proposed an original method formulated as a quadratic criterion minimization problem and solved using an iterative regularization technique. To comprehensively assess its performance, we conducted a comparative analysis with a second approach grounded in Bayesian filtering techniques.

Our comparative analysis revealed that the first approach excelled in accurately identifying failure and restart instants, even in the presence of substantial measurement noise, highlighting the effectiveness of our method. The use of the CGM in the first approach brought several advantages over traditional methods. Notably, it enabled the simultaneous identification of failures in multiple heating sources, a challenging task for conventional approaches. Additionally, the CGM ensured numerical stability, resulting in efficient and precise computations.

In the context of our study, the unique solution of the IHCP was influenced not only by the sensor placement but also significantly by the parameters and geometric configuration of the system. This aspect becomes particularly crucial in scenarios involving mobile sensors, where an iterative sensitivity analysis is vital to establish the optimum sensor trajectory. Such a positioning strategy ensures the unique solvability of the inverse problem, which is paramount for accurate and reliable failure identification.

There are several perspectives for future research following this work. One potential extension involves incorporating mobile sensors that require repositioning to enhance the precision of failure identification. In this context, the development of decision-support strategies based on predefined scenarios holds promise for further exploration.

CRediT authorship contribution statement

M.S. Bidou: Writing – original draft, Software, Methodology, Investigation, Formal analysis, Conceptualization. **L. Perez:** Writing – review & editing, Visualization, Validation. **S. Verron:** Writing – review & editing, Visualization, Validation. **L. Autrique:** Validation, Supervision, Project administration.

Declaration of competing interest

The authors declare that they have no known competing financial interests or personal relationships that could have appeared to influence the work reported in this paper.

Data availability

Data will be made available on request.

References

[1] M.-B. Cheng, V. Radisavljevic, C.-C. Chang, C.-F. Lin, W.-C. Su, A sampled-data singularly perturbed boundary control for a heat conduction system with noncollocated observation, IEEE Trans. Automat. Control 54 (6) (2009) 1305–1310.

[2] H.-N. Wu, H.-X. Li, H_∞ fuzzy observer-based control for a class of nonlinear distributed parameter systems with control constraints, IEEE Trans. Fuzzy Syst. 16 (2) (2008) 502–516, http://dx.doi.org/10.1109/TFUZZ.2007.896351.

[3] M. Krstic, A. Smyshlyaev, Boundary Control of PDEs: A Course on Backstepping Designs, SIAM, 2008.

[4] H.-N. Wu, J.-W. Wang, H.-X. Li, Exponential stabilization for a class of nonlinear parabolic PDE systems via fuzzy control approach, IEEE Trans. Fuzzy Syst. 20 (2) (2011) 318–329.

[5] M.A. Demetriou, A model-based fault detection and diagnosis scheme for distributed parameter systems: A learning systems approach, ESAIM Control Optim. Calc. Var. 7 (2002) 43–67.

[6] S. Ghantasala, N.H. El-Farra, Robust actuator fault isolation and management in constrained uncertain parabolic PDE systems, Automatica 45 (10) (2009) 2368–2373.

[7] S. Dey, H.E. Perez, S.J. Moura, Robust fault detection of a class of uncertain linear parabolic PDEs, Automatica 107 (2019) 502–510, http://dx.doi.org/10.1016/j.automatica.2019.06.014.

[8] F. Pourdadashi Komachali, M. Shafiee, Sensor fault diagnosis in fractional-order singular systems using unknown input observer, Internat. J. Systems Sci. 51 (1) (2020) 116–132.

[9] Y. Ju, X. Tian, H. Liu, L. Ma, Fault detection of networked dynamical systems: A survey of trends and techniques, Internat. J. Systems Sci. 52 (16) (2021) 3390–3409.

[10] J. Cai, H. Ferdowsi, J. Sarangapani, Model-based fault detection, estimation, and prediction for a class of linear distributed parameter systems, Automatica 66 (2016) 122–131, http://dx.doi.org/10.1016/j.automatica.2015.12.028.

[11] Y. Feng, Y. Wang, J.-W. Wang, H.-X. Li, Backstepping-based distributed abnormality localization for linear parabolic distributed parameter systems, Automatica 135 (2022) 109930, http://dx.doi.org/10.1016/j.automatica.2021.109930.

[12] Y. Lei, J. Li, A. Zhao, Spatiotemporal fault detection, estimation and control for nonlinear reaction-diffusion equations, Appl. Math. Comput. 418 (2022) 126859.

[13] H. Ferdowsi, J. Cai, S. Jagannathan, Filter-based fault detection and isolation in distributed parameter systems modeled by parabolic partial differential equations, IEEE Access (2023).

[14] M.S. Bidou, L. Perez, S. Verron, L. Autrique, Identification of failure times for a system governed by a non-linear parabolic partial differential equation, IFAC-PapersOnLine 55 (40) (2022b) 37–42, http://dx.doi.org/10.1016/j.ifacol.2023.01.045, 1st IFAC Workshop on Control of Complex Systems COSY 2022.

[15] A.N. Tikhonov, On the solution of ill-posed problems and the method of regularization, Dokl. Akad. Nauk 151 (3) (1963) 501–504.

[16] F. Yang, C.-L. Fu, A simplified Tikhonov regularization method for determining the heat source, Appl. Math. Model. 34 (11) (2010) 3286–3299.

[17] J.V. Beck, Nonlinear estimation applied to the nonlinear inverse heat conduction problem, Int. J. Heat Mass Transfer 13 (4) (1970) 703–716, http://dx.doi.org/10.1016/0017-9310(70)90044-X.

[18] G. Blanc, J.V. Beck, M. Raynaud, Solution of the inverse heat conduction problem with a time-variable number of future temperatures, Numer. Heat Transfer B 32 (4) (1997) 437–451, http://dx.doi.org/10.1080/10407799708915018, arXiv:DOI:10.1080/10407799708915018.

[19] M.N. Özisik, H.R. Orlande, Inverse Heat Transfer: Fundamentals and Applications, CRC Press, 2021.

[20] D. Givoli, A tutorial on the adjoint method for inverse problems, Comput. Methods Appl. Mech. Engrg. 380 (2021) 113810, http://dx.doi.org/10.1016/j.cma.2021.113810.

[21] M. Yin, X. Zheng, J.D. Humphrey, G.E. Karniadakis, Non-invasive inference of thrombus material properties with physics-informed neural networks, Comput. Methods Appl. Mech. Engrg. 375 (2021) 113603, http://dx.doi.org/10.1016/j.cma.2020.113603.

[22] D.V. Patel, D. Ray, A.A. Oberai, Solution of physics-based Bayesian inverse problems with deep generative priors, Comput. Methods Appl. Mech. Engrg. 400 (2022) 115428, URL https://www.sciencedirect.com/science/article/pii/S004578252200473X.

[23] F. Yang, L. Yan, T. Wei, The identification of a Robin coefficient by a conjugate gradient method, Internat. J. Numer. Methods Engrg. 78 (7) (2009) 800–816.

[24] T. Lu, W. Han, P. Jiang, Y. Zhu, J. Wu, C. Liu, A two-dimensional inverse heat conduction problem for simultaneous estimation of heat convection coefficient, fluid temperature and wall temperature on the inner wall of a pipeline, Prog. Nucl. Energy 81 (2015) 161–168.

[25] C.-H. Huang, S.-P. Wang, A three-dimensional inverse heat conduction problem in estimating surface heat flux by conjugate gradient method, Int. J. Heat Mass Transfer 42 (18) (1999) 3387–3403, http://dx.doi.org/10.1016/S0017-9310(99)00020-4.

[26] A. Vergnaud, L. Perez, L. Autrique, Adaptive selection of relevant sensors in a network for unknown mobile heating flux estimation, IEEE Sens. J. 20 (24) (2020) 15133–15142, http://dx.doi.org/10.1109/JSEN.2020.3009779.
[27] Z. He, F. Ni, W. Wang, J. Zhang, A physics-informed deep learning method for solving direct and inverse heat conduction problems of materials, Mater. Today Commun. 28 (2021) 102719, http://dx.doi.org/10.1016/j.mtcomm.2021.102719.
[28] O.M. Alifanov, Iterative regularization of inverse problems, in: Inverse Heat Transfer Problems, Springer Berlin Heidelberg, Berlin, Heidelberg, 1994, pp. 227–328, http://dx.doi.org/10.1007/978-3-642-76436-3_9.
[29] C.-W. Lu, M.R. Reynolds Jr., EWMA control charts for monitoring the mean of autocorrelated processes, J. Qual. Technol. 31 (2) (1999) 166–188.
[30] A. Vergnaud, L. Perez, L. Autrique, Quasi-online parametric identification of moving heating devices in a 2D geometry, Int. J. Therm. Sci. 102 (2016) 47–61.
[31] Y. Jarny, M. Ozisik, J. Bardon, A general optimization method using adjoint equation for solving multidimensional inverse heat conduction, Int. J. Heat Mass Transfer 34 (11) (1991) 2911–2919, http://dx.doi.org/10.1016/0017-9310(91)90251-9, URL https://www.sciencedirect.com/science/article/pii/0017931091902519.
[32] V.A. Morozov, Methods for Solving Incorrectly Posed Problems, Springer Science & Business Media, 2012.
[33] M.S. Bidou, S. Verron, L. Perez, L. Autrique, Kalman smoother for detection of heat sources defects, in: 2022 International Conference on Control, Automation and Diagnosis, ICCAD, 2022a, pp. 1–6, http://dx.doi.org/10.1109/ICCAD55197.2022.9853959.
[34] M.S. Bidou, S. Verron, L. Perez, L. Autrique, Bayesian filter for failure times identification of moving heat sources in 2D geometry, Internat. J. Systems Sci. (2023) 1–16.
[35] J. Kaipio, E. Somersalo, Statistical and Computational Inverse Problems, in: Applied Mathematical Sciences, Springer New York, 2006, URL https://books.google.fr/books?id=h0i-Gi4rCZIC.
[36] J.P. Kaipio, C. Fox, The Bayesian framework for inverse problems in heat transfer, Heat Transf. Eng. 32 (9) (2011) 718–753, http://dx.doi.org/10.1080/01457632.2011.525137, arXiv:DOI:10.1080/01457632.2011.525137.
[37] M.N. Özişik, H.R. Orlande, M.J. Colaco, R.M. Cotta, Finite Difference Methods in Heat Transfer, CRC Press, 2017.
[38] H.E. Rauch, F. Tung, C.T. Striebel, Maximum likelihood estimates of linear dynamic systems, AIAA J. 3 (8) (1965) 1445–1450.
[39] K.P. Murphy, Machine Learning: A Probabilistic Perspective, MIT Press, 2012.